RESEARCH ARTICLE

Figures and figure supplements

MicroRNA-218 instructs proper assembly of hippocampal networks

Seth R Taylor *et al*.

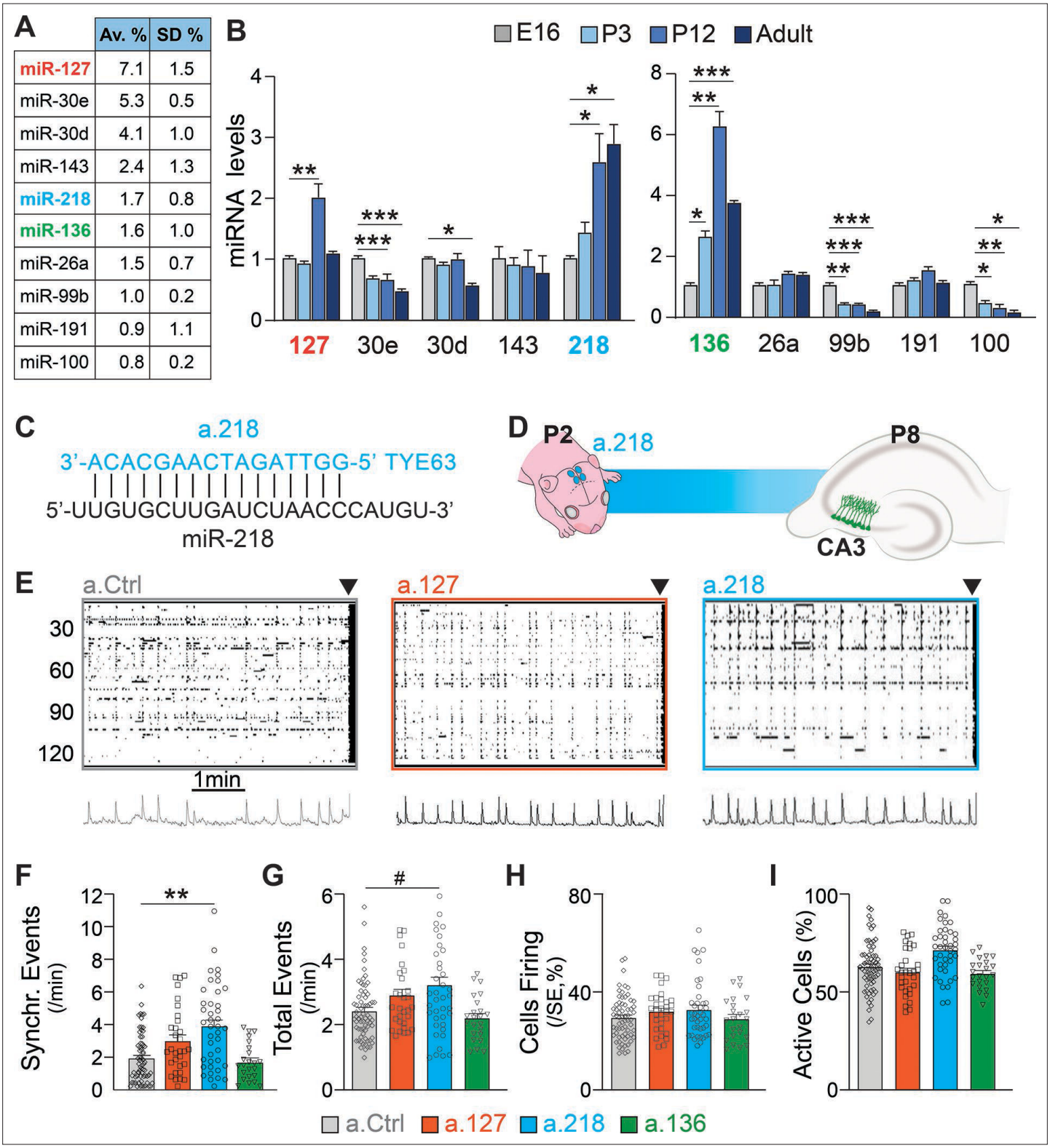

Figure 1. Inhibition of the developmentally regulated miRNA miR-218 alters spontaneous neuronal activity in early postnatal life. (**A**) Abundance of a subset of highly expressed miRNAs in the developing hippocampus (data averaged for 6 C57BL/6J P12 animals) expressed as percentage of total sequenced reads obtained from small RNA deep sequencing (Illumina). Data come from ***Lippi et al., 2016***. N=6 mice. (**B**) Developmental regulation of 10 abundant miRNAs measured by miRNA qPCR. Bar graphs represent the abundance of each miRNA at P3, P12, and adult (>P40), normalized first for housekeeping gene *Snord45b* (available from Thermofisher under name: snoRNA412) and then for the amount present at E16. MiR-127, miR-218,

Figure 1 continued on next page

Figure 1 continued

and miR-136 increased in expression during early postnatal development. Note: well-studied miRNAs (i.e. miR-124) were not tested here. N=3–5 / time point. Statistics were calculated from a full mixed effects model with miRNA and age as fixed effects and animal as a random effect, followed by post-hoc tests with FDR multiple testing correction. (**C**) Illustration showing the complementarity of a-218 with miR-218 (vertical bars indicating the complementary bases) which is essential for the inhibition. (**D**) Schematic of the time course of miR-218 inhibition, starting at P2, and calcium imaging performed at P8 in the CA3 hippocampal region. (**E**) Raster plots of neuronal activity in movies of animals injected with a.Ctrl (left), a.127 (center), and a.218 (right). The principal component analyses of population activity are shown below to identify the SEs. (**F–I**) MiR-218 inhibition increased the number of SEs (**F**, p=0.0019 for miR-218). MiR-218 inhibition increased total events (**G**, p=0.0625), but did not change the percentage of cells in SEs or that are active (**H–I**). MiR-136 or miR-127 inhibition had no effect on spontaneous activity. Bar graphs: mean ± SEM; Outliers detected with ROUT in GraphPad Prism (Q=1%) and removed. Statistics were calculated from a linear mixed model accounting for animal as a random effect, with Dunnett's multiple comparisons test. #p<0.1, *p<0.05, **p<0.01, ***p<0.001, N for a.Ctrl=69 movies/19 animals; a.136=23 movies/5 animals; a.127=31 movies/7 animals; a.218=41 movies/8 animals.

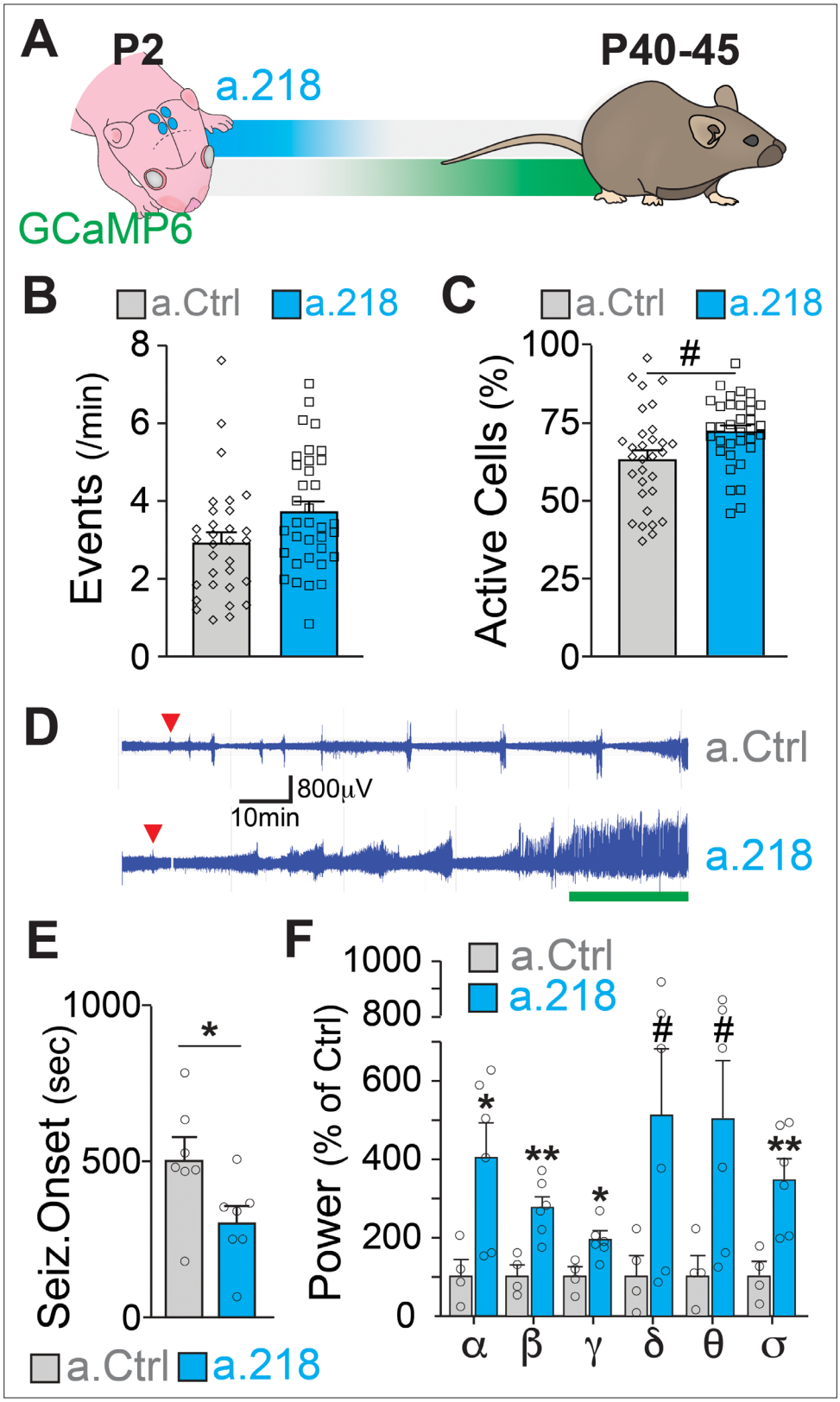

Figure 2. MiR-218 inhibition in early postnatal life causes long-lasting deficits in network activity. (**A**) Schematic of the timeline of miR-218 inhibition and of GCaMP6f expression. (**B**) Quantification of calcium activity showed no changes in the number of events (p-value = 0.1976) and (**C**) an increase in the percentage of active cells (p-value = 0.05562) in slices from P40-45 animals injected on P2. For B and C, linear mixed model accounting for animal as

Figure 2 continued on next page

Figure 2 continued

a random effect. N for a.Ctrl=31 movies from 5 animals, N for a.218=35 movies from 5 animals. (**D–F**) KA-induced seizures at ~P40 start earlier in a.218-treated mice. (**D**) EEG recordings immediately after KA. a.218 mice show stronger responses. The green line denotes continuous status epilepticus, a sign of a pathological network activity. Red triangle: first seizure (confirmed by behavior). a.218 mice show faster seizure onset, N=7 mice/group, unpaired t-test (**E**) and increased power at many frequencies (**F**), N=4–6mice/ group, unpaired t-tests. Bar graphs: mean ± SEM; #p<0.1, *p<0.05, **p<0.01. α: alpha, β: beta, γ: gamma, δ: delta, θ : theta, σ: sigma.

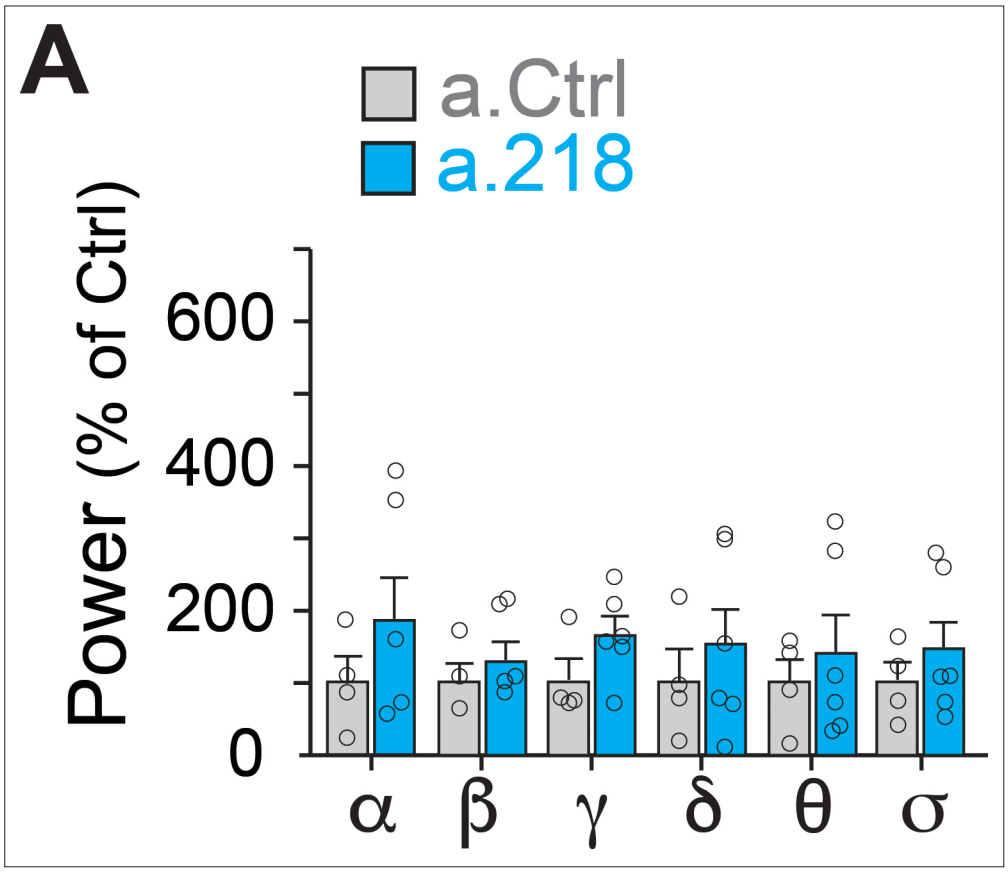

Figure 2—figure supplement 1. Early life inhibition of miR-218 has no effect on baseline power before the KA challenge. N=4–6mice/ group. Bar graphs: mean ± SEM; α: alpha, β: beta, γ: gamma, δ: delta, θ : theta, σ: sigma.

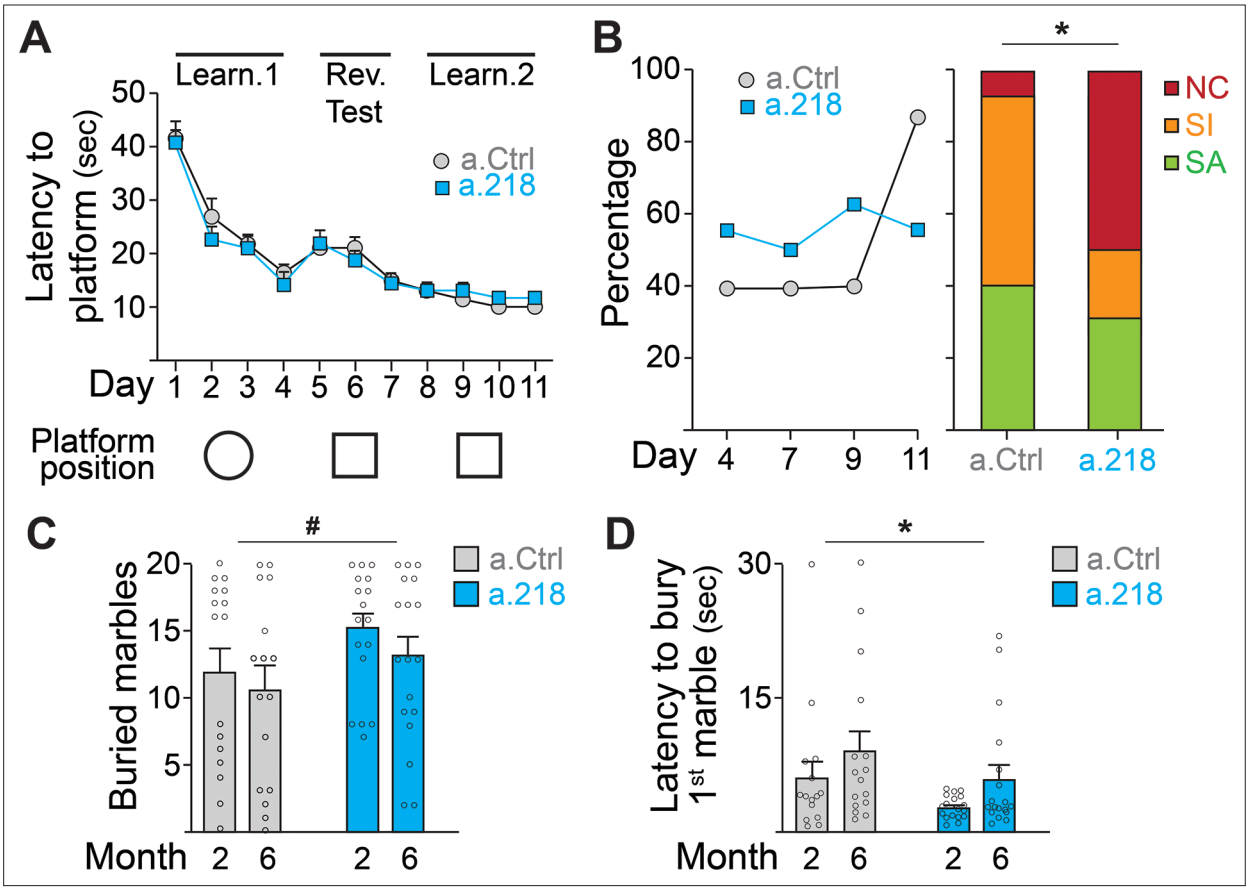

Figure 3. MiR-218 inhibition causes selective behavioral changes. (**A–B**) Morris water maze. (**A**) The learning curve did not demonstrate any statistically significant differences between experimental groups (repeated-measures ANOVA, Time F (10, 290) p=0.0001, Treatment F (1, 29) p=0.7167, Time x Treatment F (10, 290) p=0.7843). The ability to discriminate between similar contexts (reversal test, days 5 and 6) appeared preserved in a.218 mice (repeated-measures ANOVA, Time F (1, 29) p=0.7595, Treatment F (1, 29) p=0.2183, Time x Treatment F (1, 29) p=0.3450). Similarly, the latency for the first entry on platform location in the probe test did not differ between the two groups (p=0.3862). (**B**) Search strategy analysis showed an increase in spatially targeted strategies during learning phase and probe test for a.Ctrl compared to a.218 mice (Fisher's test, p=0.02). NC: non cognitive; SI: spatial inaccurate; SA: spatial accurate. (**C–D**) Marble burying Test. a.218 mice showed an increase in the number of buried marbles (**C**) (2 months vs 6 months; repeated measures ANOVA, F (1, 31)=4.074, p=0.052) and a reduced latency to bury the first marble (**D**) (2 months vs 6 months; repeated measures ANOVA, F (1, 31)=6.257, p=0.018). Bar graphs: mean ± SEM; #p<0.1, *p<0.05. N=16–18 mice/group.

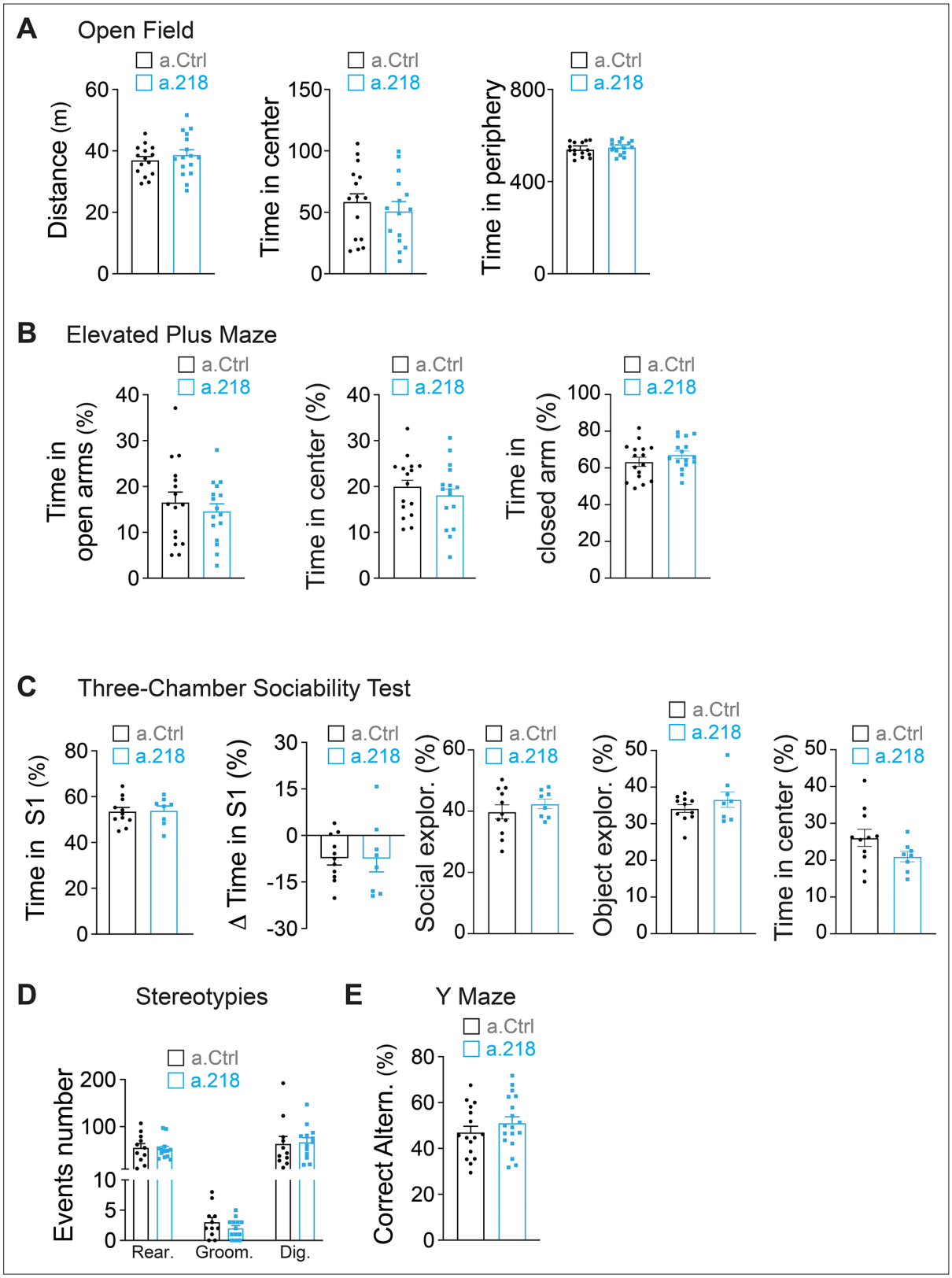

Figure 3—figure supplement 1. Early life inhibition of miR-218 has no effect on several behavioral measures. No effects of miR-218 inhibition with a.218 were seen in the open field (**A**), elevated plus maze (**B**), Y-maze (**C**), three-chamber sociability test (**D**) or in the number of stereotypies (**E**). N=16 mice/group. Bar graphs: mean ± SEM; explor.: exploration; Rear.: rearing; Groom.: grooming; Dig.: digging.

Figure 4. Spatial and temporal distribution of miR-218 expression and inhibition. (**A–B**) MiR-218 and miR-124 expression in developing mouse brain. (**A**) Optical microscopy images of fresh frozen brain slices labelled with miR-218 and miR-124 LNA ISH probes represented by dark staining due to NBT/BCIP precipitation. MiR-218 is detected in the CA1, DG, and CA3 regions of the hippocampus. MiR-218 expression changes during hippocampal maturation from a low level at P2 that increases at P7 and then remains stable in the adult (P60). MiR-124, a highly abundant neuronal miRNA, is used at P60 as positive control. Scale bar = 100 µm. (**B**) Confocal microscopy images of fresh frozen brain slices labelled with miR-218 LNA probes (green), DAPI (blue) and anti-GFAP or anti-NeuN antibodies (red). Top: representative panels of miR-218 expression in cortex, corpus callosum (CC) and hippocampus (CA1, CA3). Scale bar = 50 µm. Bottom left: high magnification images showing single cells from the corpus callosum. Green and red colocalization is marked by yellow color (arrows). Bottom right: high magnification images showing neuronal cells from CA1 and CA3. Green spots are localized inside neuronal cells labelled in red. Scale bar = 10 µm. (**C**) Schematic of *Mir218-1* gene located in *Slit2* (intron 15) and *Mir218-2* gene located in *Slit3* (intron 13). The prevalent mature miR-218 sequence (5 p) is identical between the two genes. However, the second base downstream the 3′ end of the 5 p sequence is G in *Mir218-2* (purple arrow) and C in *Mir218-1*. The less abundant miR-218–3 p sequences differ in multiple bases between the genes (purple arrows). (**D**) Small RNA-Seq data were used to detect C or G at the second base downstream the 3′ end of the 5 p sequence. G (*Mir218-2*) is much more frequent. (**E**) Similarly, miR-218-2-3p is more abundant than miR-218-1-3p. (**F**) MiR-218 levels in P15 *Mir218-1* KO animals are

Figure 4 continued on next page

Figure 4 continued

not significantly different from WT controls. In contrast, loss of one *Mir218-2* allele causes a 50% reduction in miR-218 levels. N=3–7 animals/genotype, adjusted p=0.002, Kruskal-Wallis test with Dunn's multiple comparisons test. (**G**) Lentiviral miRNA sensors demonstrate that miR-218 is abundant in vivo and can be blocked by a.218. Top, scheme of the lentiviral construct encoding the miR-218 sensor (8 x perfectly complementary miR-218 MREs cloned downstream of a far-red fluorescent protein, RFP_{670}). Bottom, CA1 region in mice injected with the sensor and either non-fluorescent a.Ctrl (top) or a.218 (Bottom). a.218 rescues RFP_{670} fluorescence. Scale bar = 10 μm. (**H**) Quantification of RFP_{670} normalized for GFP. All values are expressed relative to a control sensor lacking miR-218 MREs in which RFP_{670} fluorescence is not repressed by miR-218 (RFP_{670} /GFP = 1). 8 x miR-218 MREs strongly reduce RFP_{670} fluorescence in the presence of a.Ctrl. RFP_{670} fluorescence declines with age, reflecting the developmental increase in miR-218 expression. At P8 and P15, a.218 rescues RFP_{670} fluorescence to levels similar to the control sensor, indicating effective inhibition of miR-218. The inhibition is strongly decreased by P26. At P8, N=14 sections/3 animals (a.Ctrl) and 23 sections/3 animals (a.218). At P15, N=16 sections/3 animals (a.Ctrl) and 15 sections/4 animals (a.218). At P26, N=11 sections/4 animals (a.Ctrl) and 31 sections/6 animals (a.218). Bar graphs: mean ± SEM; linear mixed model with age and antagomir as fixed effects accounting for animal as a random effect with Tukey adjustment for multiple comparisons. *p<0.05, ***p<0.001.

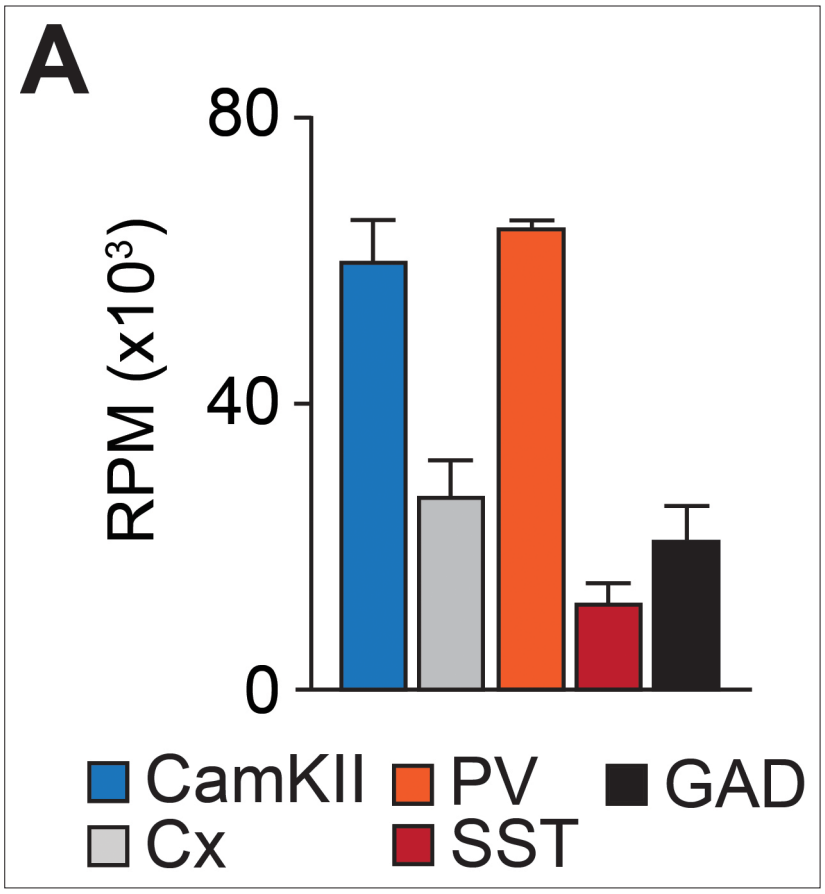

Figure 4—figure supplement 1. MiR-218 is enriched in CaMKII +PNs and PV +INs. Expression of miR-218 in specific cell types from P56 mouse neocortex. Data from ***He et al., 2012***. Bar graphs: mean ± SEM.

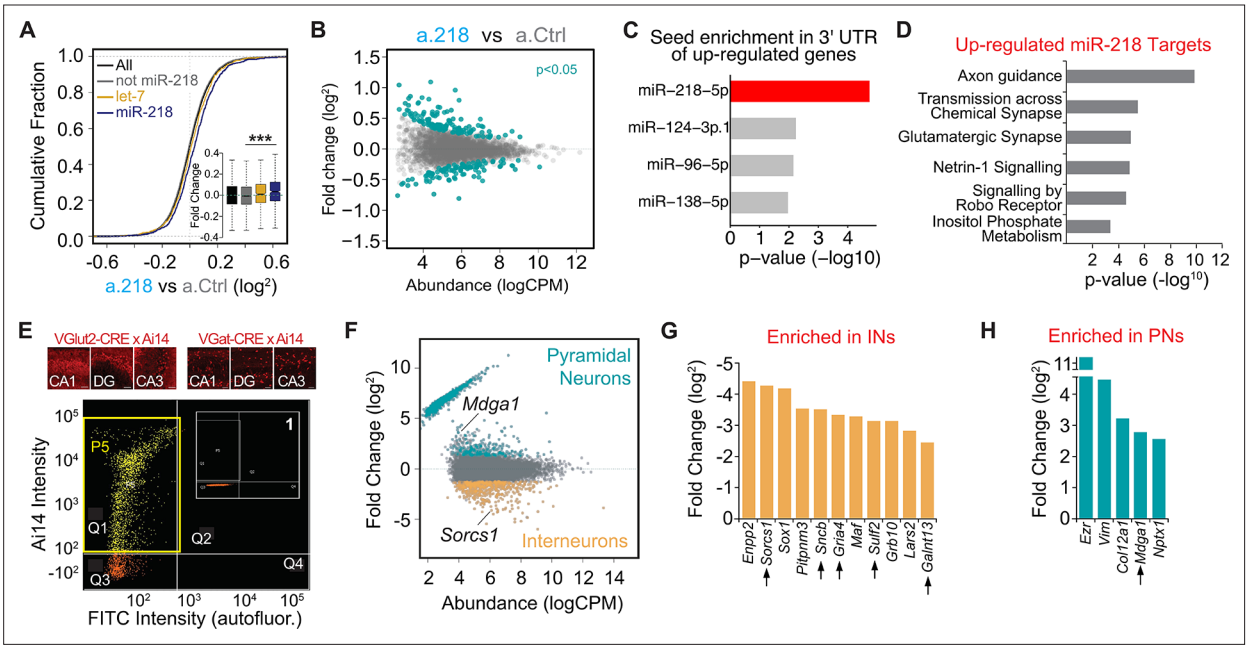

Figure 5. Mapping miR-218 targets and transcriptional changes upon miR-218 inhibition with RNA-Seq from dorsal hippocampus at P8. (**A**) Cumulative fraction of all genes (black line), non miR-218 targets (gray line), let-7 targets (yellow), miR-218 targets purple. Fold change of this subset of genes in the insert (bottom right). ***p<9.7e-12 (KS-test). (**B**) MA plot (Abundance vs Fold Change) of transcriptional changes in a.218 mice compared to a.Ctrl littermates. Green dots represent upregulated (top, p<0.05) or downregulated genes (bottom, p<0.05). N=3 mice/group. (**C**) MiRNA seed enrichment analysis of up-regulated genes (p<0.05). The MRE for miR-218 is significantly enriched, suggesting that the list of upregulated genes contains bona fide miR-218 targets. (**D**) GO term analysis of all upregulated predicted miR-218 target genes (391 genes). (**E**) FACS of VGluT2-CRE/Ai14 or VGAT-CRE/Ai14 dorsal hippocampi. Top: representative images of Ai14 positive PNs (top row) or INs in CA1, DG, and CA3 at P8. Bottom: two-dimensional scatterplot illustrating FACS isolation of PNs. Ai14 fluorescence intensity is displayed on the Y axis and FITC (autofluorescence) is on the X axis. Sorted VGluT2-CRE/Ai14 PNs are shown as yellow dots. The P5 yellow rectangle (in quarter Q1) delimits the area chosen for sorting. Insert (1) shows the same gating for CRE negative neurons, where the P5 gate is empty. Scale bar = 50 μm. (**F**) MA plot of transcriptional differences between PNs (VGluT2-CRE/Ai14) and INs (VGAT-CRE/Ai14) showing genes significantly up-regulated in PNs and INs. (**G–H**) Genes upregulated in a.218 vs a.Ctrl (p<0.05) and significantly enriched (FDR <0.05) in either INs (**G**) or PNs (**H**). Black arrows denote predicted miR-218 targets.

Figure 5—figure supplement 1. Validation of a.218 and identification of miR-218 targets. (**A**) miR-218 expression levels in the dorsal hippocampus of a. Ctrl and a.218 mice used for RNA-Seq showing efficient inhibition of miR-218. (**B**) Small RNA-Seq of a.Ctrl and a.218 mice reveals significant blockade of miR-218 and upregulation of several miRNAs. (**C**) GO terms enriched in genes up-regulated (logFC >0.1, p-value <0.2) in dorsal hippocampus of a.218 vs a.Ctrl. Note several terms relating to synaptic formation and function and neuronal excitability. (**D–F**) RNA-Seq of *Mir218-1*$^{-/-}$; *Mir218-2*$^{+/-}$ mice vs WT littermates. (**D**) MA plot of transcriptional changes in *Mir218-2*$^{+/-}$ mice compared to WT controls. Red dots represent genes significantly (p<0.05) upregulated (top) or downregulated (bottom). (**E**) miRNA seed enrichment in genes up-regulated in the dorsal hippocampus of *Mir218-1*$^{-/-}$; *Mir218-2*$^{+/-}$ mice vs WT littermates. (**F**) Cumulative fraction of fold change values for all genes (black), predicted miR-218 targets (blue) and non miR-218 targets (gray). (**G**) Venn diagram displaying the overlap in predicted miR-218 targets up-regulated in a.218 vs a.Ctrl and *Mir218-1*$^{-/-}$; *Mir218-2*$^{+/-}$ vs WT littermate

Figure 5—figure supplement 1 continued on next page

Figure 5—figure supplement 1 continued

experiments. (**H**) Up-regulated genes from a.218 vs a.Ctrl RNA-Seq (138 genes, p-value <0.05) were enriched in several single-cell RNA-Seq clusters from early postnatal mouse brain and spinal cord (P2 and P11). Single-cell data from ***Rosenberg et al., 2018***. GABAergic neuron clusters (*Gad1*/*Gad2* expressing) are colored light orange, excitatory glutamatergic hippocampal neuron cluster in teal, and light green denotes excitatory glutamatergic neurons from brain regions other than the hippocampus. Enrichment was tested using the hypergeometric test. Up-regulated genes from LNA RNA-seq displayed significant enrichment (FDR <0.01) in all clusters shown.

Figure 6. MiR-218 inhibition induces selective structural changes. (**A**) Immunostaining of VGAT (red) and Gephryn (green) in the stratum pyramidale of the hippocampal CA3 region at P8. Scale bar = 10 µm. (**B**) Quantification of co-localized puncta (yellow). N for a.Ctrl=11 sections/3 mice, for a.218=12 sections/3 mice. (**C**) Traces of mIPSC and mEPSC recordings in CA3 PNs at P14-P16. (**D**) Quantification of mIPSC and mEPSC amplitude and frequency in a.218 vs a.Ctrl mice. N=14–17 cells from 4 to 6 mice/group C. (**E–F**) Analysis of dendritic spines on secondary proximal dendrites in CA1 and CA3 at P11 and P50. a.218 induces a decrease in spines in CA1 that persists in the adult. Scale bar = 1 µm. N=5–6 mice/group. Bar graphs: mean ± SEM; ⋆p<0.05. Statistics were calculated using linear mixed models accounting for animals (**B and D**), and unpaired t-tests (**F**).

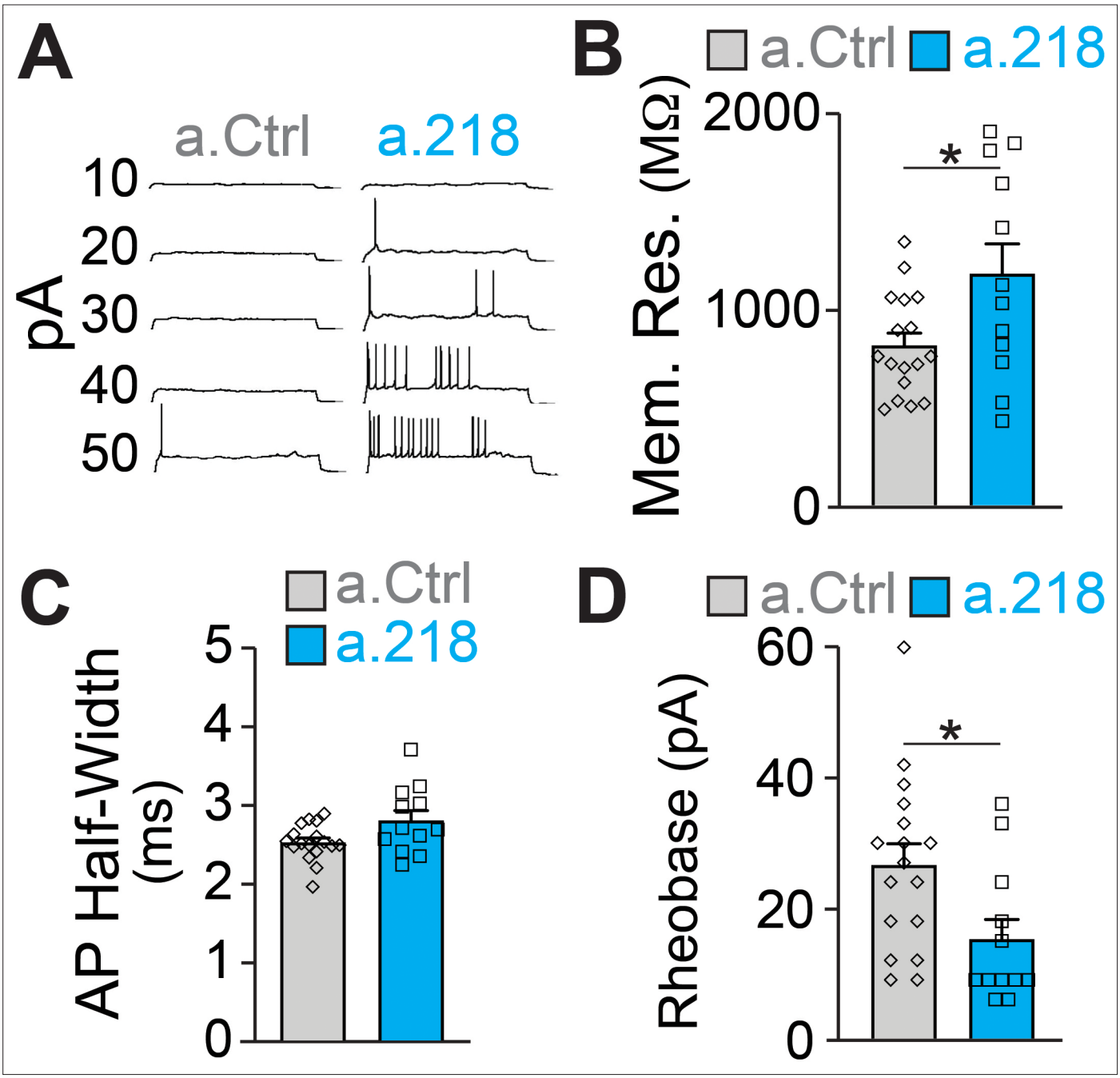

Figure 7. MiR-218 inhibition induces changes in neuronal intrinsic properties. (**A**) Traces of whole-cell current clamp recordings of CA3 PNs in acute slices from a.Ctrl (left) and a.218 (right) mice showing spiking in response to current injection. a.218 increases membrane resistance (**B**), has no effect on action potential (AP) half-width (**C**), and reduces rheobase (**D**) compared to a.Ctrl. N for a.Ctrl=17 cells/9 mice; for a.218, N=12 cells/9 mice. Bar graphs: mean ± SEM; *p<0.05. All statistics are calculated from linear mixed models accounting for animals as a random effect.

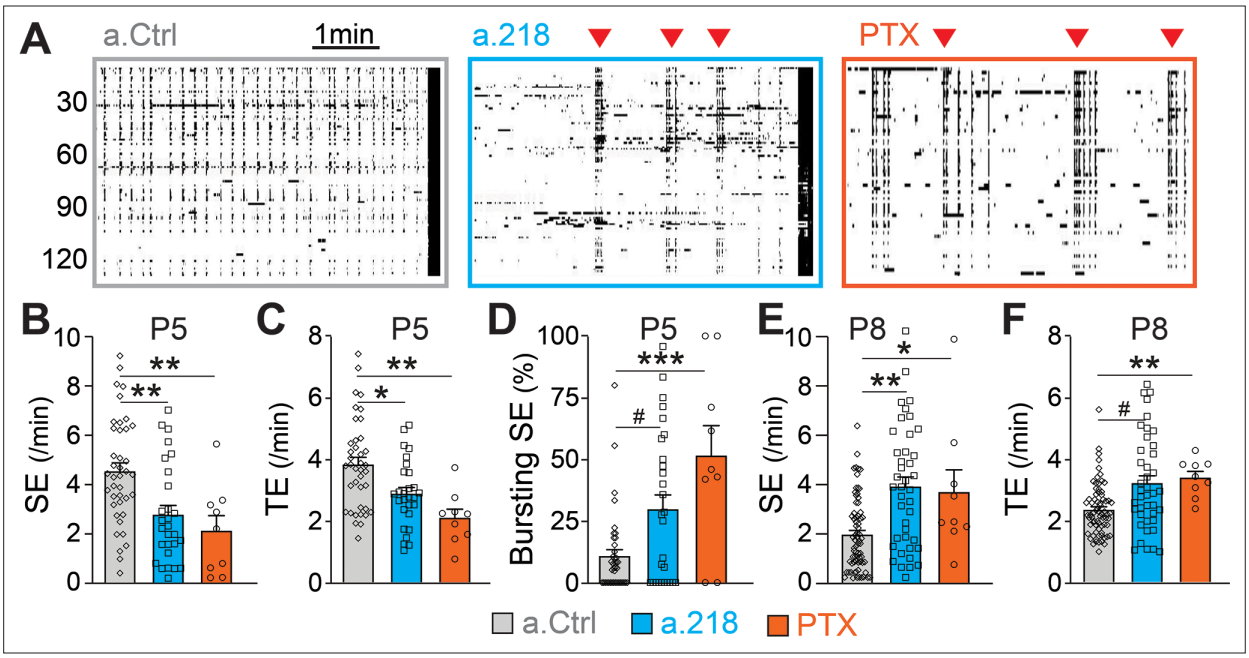

Figure 8. MiR-218 inhibition alters GABAergic neurotransmission at P5. (**A**) Raster plots of neuronal activity in movies from P5 a.Ctrl mice, a.218 mice, or slices from WT mice treated with picrotoxin (PTX). Each line is a cell, black dots represent calcium spikes. Black vertical lines indicate SEs. Red triangles indicate bursts of SEs. a.218 mice and PTX slices show fewer SEs (**B**) and total events (TE, **C**) that tend to occur in bursts (**D**). N=36 movies/ 5 animals (a.Ctrl), 28 movies /5 animals (a.218), 9 movies/3 animals (PTX). (**E–F**) In contrast to P5, at P8 both a.218 and PTX increase the frequency of SEs (**E**) and total events (**F**). a.218 data and comparisons in (**E–F**) are from ***Figure 1F–G***. N=9 movies/3 animals (PTX). Bar graphs: mean ± SEM; #p<0.1, **p<0.01, ***p<0.001. We fit linear mixed models accounting for animal as a random effect between PTX and a.Ctrl conditions at P5 and P8 or a.Ctrl and a.218 conditions at P5.

Figure 9. *Mir218-2* cKO in INs but not in PNs alters long-term network stability. MiR-218 was quantified in VGluT2-Cre/Ai14/*Mir218-2*$^{fl/fl}$ (**A**) and VGAT-Cre/Ai14/*Mir218-2*$^{fl/fl}$ (**B**) using FACS followed by qPCR. N=3 animals/group (**C**) Decrease in miR-218 function was confirmed with a miR-218 sensor (see ***Figure 4G*** for details about the sensor) for both PNs and INs. N=8–12 sections from 3 mice/group. Scale bar = 50 µm. (**D**) VGAT-Cre/Ai14/*Mir218-2*$^{fl/fl}$ mice show faster seizure onset after KA delivery, while VGluT2-Cre/Ai14/*Mir218-2*$^{fl/fl}$ show no differences. (**E**) VGAT-Cre/Ai14/*Mir218-2*$^{fl/fl}$ mice show longer seizure duration, while VGluT2-Cre/Ai14/*Mir218-2*$^{fl/fl}$ mice show no differences. N=9–18 mice/group. (**F**) Marble burying test shows no differences between VGAT-Cre/*Mir218-2*$^{fl/fl}$ mice and littermate controls. Two-way ANOVA with Tukey's multiple comparison test (**A**), unpaired t-test (**B**), linear mixed models accounting for animals as a random effect and age as a fixed effect (**C**), Mann-Whitney test (**D–F**). Bar graphs: mean ± SEM; *p<0.05, **p<0.01.

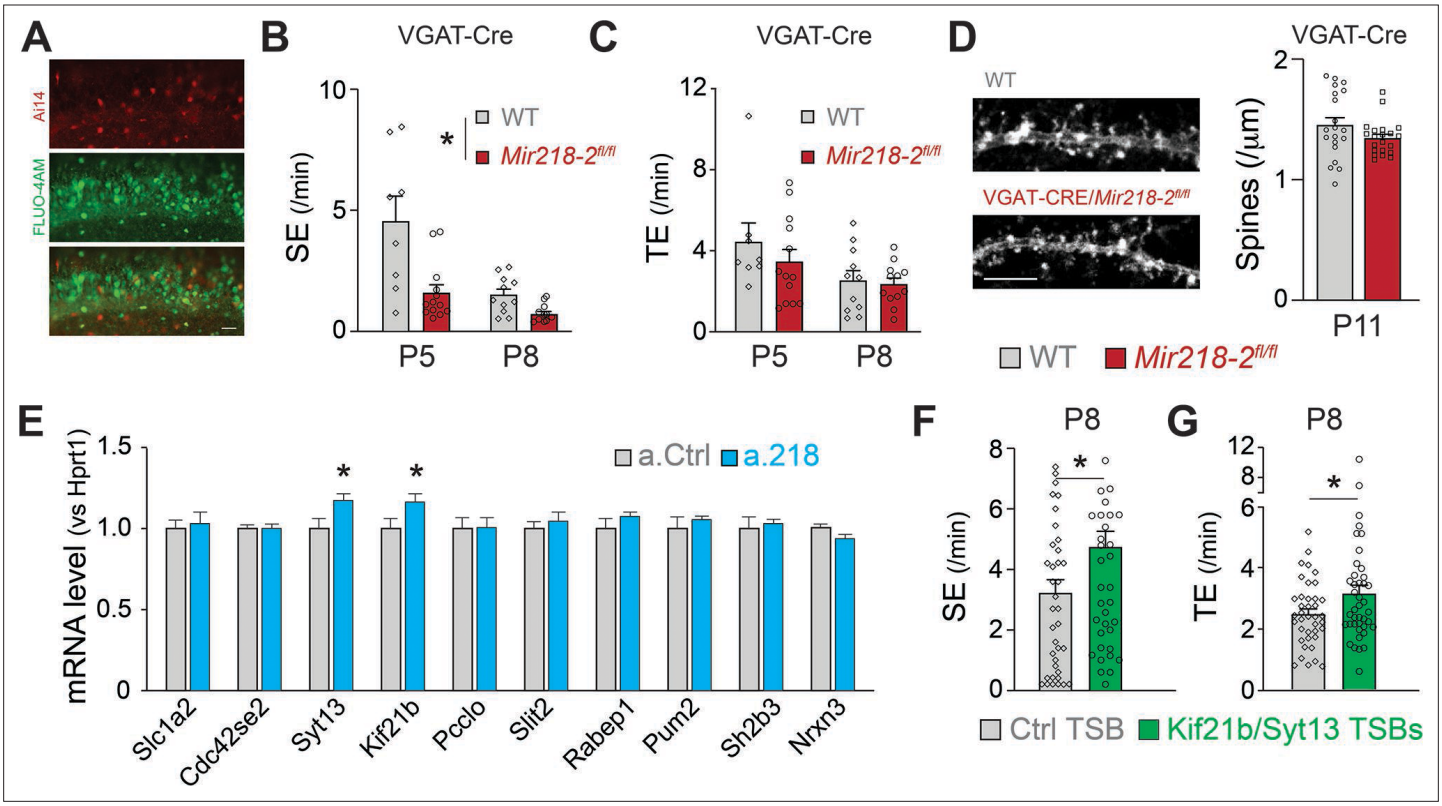

Figure 10. Cellular and molecular mechanisms leading to altered spontaneous network activity. (**A**) Images of VGAT-Cre/Ai14/*Mir218-2*$^{fl/fl}$ slices used for calcium imaging, showing INs (top, red) in which Cre recombination occurred and PNs loaded with FLUO-4AM (middle, green). Scale bar = 50 µm. (**B**) SEs are decreased in VGAT-Cre/*Mir218-2*$^{fl/fl}$ mice vs littermate controls. N=2–6 movies/3 animals per condition. (**C**) No changes in TEs. (**D**) No changes in CA1 PN spine density at P11 in VGAT-Cre/*Mir218-2*$^{fl/fl}$ mice. N=4–17 dendrites/2–3 animals per condition. Scale bar = 5 µm. (**E**) *Syt13* and *Kif21b* are significantly upregulated in the hippocampi of a.218-treated mice. N=3 animals per condition. (**F–G**) *Kif21b* and *Syt13* TSBs induce an increase in SEs and TEs. N for Ctrl TSB = 39 movies/8 animals, for *Kif21b/Syt13* TSBs 41 movies/7 animals. Statistics for B, and C are derived from linear mixed models accounting for animals as a random effect and age as a fixed effect. Statistics for F, and G are derived from linear mixed models accounting for animals as random effects. Bar graphs: mean ± SEM. *p<0.05.